Robust Frequency-Shifting Based Control Amid False Data Injection Attacks for Interconnected Power Systems With Communication Delay

Nikhil Kumar, Pulakraj Aryan, *Graduate Student Member, IEEE*, G. Lloyds Raja, *Member, IEEE*, and Utkal Ranjan Muduli, *Senior Member, IEEE*

***Abstract*—Communication delays and false data injection attacks pose significant threats to the frequency control of automatic generation systems. This article presents a Golden Jackal Optimizer (GJO)-enhanced frequency-shifted internal model control (FIMC) scheme aimed at addressing these challenges in a dual-area thermal power system. The FIMC approach employs a pole and zero shifting variable that acts as a system robustness indicator. The article determines an analytical search range for this variable using the Routh-Hurwitz criteria, which were later utilized by GJO. The robustness and performance of the GJO-tuned FIMC are tested against random and step load disturbances, as well as system nonlinearities. The article models various false data injection threats, assessing the effectiveness of the GJO-tuned FIMC in neutralizing these threats under inherent communication delays. Finally, the proposed strategy is verified in real-time through hardware, employing the OPAL-RT platform. The results are compared with a recent strategy, underscoring the advanced efficacy of the proposed approach.**

***Index Terms*—Communication delays, false data injection attacks, Golden Jackal Optimizer (GJO), interconnected power systems internal model control (IMC).**

NOMENCLATURE

B_i	Frequency bias parameter.
ACE_i	Area control error.
R_i	Speed regulation constant.
τ_{gi}	Governor time constant.
τ_{ti}	Turbine time constant.
δ_i	Frequency sensing load coefficient.
H_i	Inertia constant.
R_i	Droop coefficient.
ΔP_{tie}	Change in tie-line power.
Δf_i	Change in frequency.
ΔP_{Li}	Change in load demand.
ψ_i	Frequency shifting adjustment parameter.
T_s	Settling Time.
PSO	Particle Swarm Optimization.
LFC	Load Frequency Control.
P	Proportional.
PI	Proportional-Integral.
PID	Proportional-Integral-Derivative.
IMC	Internal Model Control.
PIDD2	Proportional-Integral-Double-Derivative.
CPS	Cyber-physical System.
EO	Equilibrium Optimizer.
AO	Arithmetic Optimizer.
AVOA	African Vulture Optimization Algorithm.
DoS	Denial-of-Service.
FDI/FDIA	False Data Injection/FDI Attack.
FIMC	Frequency-shifted Internal Model Control.
GJO	Golden Jackal Optimizer.
ITSE	Integrated Time Square Error.
IAE	Integrated Absolute Error.
ITAE	Integrated Time-weighted Absolute Error.
MOF	Multi-Objective Function.
HIL	Hardware-in-loop.
SLD	Step Load Disturbance.
RLD	Random Load Disturbance.
GDB	Governor Dead Band.
BD	Boiler Dynamics.
MOS	Maximum Overshoot.
MUS	Maximum Undershoot.
RH	Routh-Hurwitz.

Manuscript received 27 September 2023; revised 24 November 2023; accepted 27 December 2023. Date of publication 1 January 2024; date of current version 21 March 2024. Paper 2023-IACC-1195.R1, presented at the 2022 IEEE Global Conference on Computing, Power and Communication Technologies, New Delhi, India, Sep. 23–25, and approved for publication in IEEE TRANSACTIONS ON INDUSTRY APPLICATIONS by the Industrial Automation and Control Committee of the IEEE Industry Applications Society [DOI: 10.1109/GlobConPT57482.2022.9938319]. *(Corresponding authors: Pulakraj Aryan; G. Lloyds Raja; Utkal Ranjan Muduli.)*

Nikhil Kumar, Pulakraj Aryan, and G. Lloyds Raja are with the Department of Electrical Engineering, National Institute of Technology, Patna 800005, India (e-mail: nik.06jan@gmail.com; pulakraj258@gmail.com; lloyd.raja@gmail.com).

Utkal Ranjan Muduli is with Advanced Power and Energy Center (APEC), Department of Electrical Engineering and Computer Science, Khalifa University, Abu Dhabi 127788, UAE (e-mail: utkal.muduli@ku.ac.ae).

Color versions of one or more figures in this article are available at https://doi.org/10.1109/TIA.2023.3348775.

Digital Object Identifier 10.1109/TIA.2023.3348775

I. INTRODUCTION

LOAD Frequency Control (LFC) plays a crucial role in maintaining the stability of interconnected power systems by regulating system frequency and managing tie-line power deviations under variable load demands. Recent studies [1], [2] highlight the growing challenges in LFC due to emerging factors such as communication delays and cyberattacks, which threaten the stability of the system and the synchronous

operation of the generator units. Although traditional control approaches, including proportional (P), proportional-integral (PI), and proportional-integral-derivative (PID) controllers, are foundational in LFC, their vulnerability to cyber-attacks necessitates the exploration of enhanced control strategies. Recent advances have focused on augmenting these traditional controllers with innovative features, such as hybridization with two or three degrees of freedom [3], the implementation of fractional order controllers [4], and the integration with cascade and fuzzy logic-based controllers [5]. Despite these advances, PID controllers remain prominent in industrial applications due to their simplicity and ease of implementation, as discussed in the current literature [2], [6]. This backdrop sets the stage for our research, which aims to address the challenges posed by communication delays and cyber-attacks in LFC, exploring robust control solutions that can enhance system resilience while balancing the need for simplicity and practical applicability in industrial settings.

In the field of LFC, there has been a significant shift toward the application of metaheuristic approaches, with the aim of improving control effectiveness and adaptability. Notable developments include the Gravitational Search Algorithm-Based State Feedback Controller [7], Quasi-oppositional Equilibrium Optimizer (EO) [5], Arithmetic Optimizer (AO) [4], and the African Vulture Optimization Algorithm (AVOA) [8]. However, these advanced strategies have often been constrained by arbitrary search ranges, as pointed out in recent literature [2], [6], which may limit their optimization potential. On the contrary, a promising trend is the integration of metaheuristic methods with analytical design techniques. This combination leverages the initial analytical search range provided by traditional methods, thereby enhancing the efficiency of the optimization process and reducing the risk of convergence to local minima. Analytical LFC strategies, including the PID design based on internal model control (IMC) and its variants, have gained traction [9], [10]. Techniques such as Kharitonov-theorem-based strategies [11], direct synthesis [12], and frequency domain-based strategies [13] have been explored. A notable example is the recent development of an IMC-based robust proportional integral double derivative (PIDD2) controller integrated with maximum sensitivity specifications [9]. However, these methods often require trial and error to adjust the parameters, highlighting the need for more systematic approaches. The integration of metaheuristic optimizers with analytically designed controllers represents a significant step forward, as evidenced by recent research [14]. This approach offers a more structured and potentially effective method of adjusting the control parameters, which presents a promising direction for future advancements in LFC technology.

The secure and stable operation of interconnected cyber-physical systems (CPS) faces significant threats from the prevalence of cyber-attacks and communication delays [15], [16]. These challenges can disrupt the coordination within the integrated network of distribution systems, remote terminal units, power plants, and communication channels, adversely affecting power quality [17], [18]. To counteract these threats, various strategies have been developed. For instance, dynamic event-triggered mitigation techniques using Lyapunov stability theory have been employed to address denial of service (DoS) and deception attacks [19]. Furthermore, a H_∞-based LFC scheme was formulated to combat false data injection (FDI) and DoS attacks [20]. Other notable methods include resonance principle-based strategies for evading detection [21], observer-based PI controllers for random joint attacks [22], and state-space-based PI controllers, designed using Lyapunov stability and linear matrix theories, to handle FDI and DoS attacks with time-varying delays [23]. Most recently, a resilient control strategy based on an extended observer-based state was reported for industrial processes [24]. These developments represent significant steps toward improving the resilience of CPSs against cyber threats. However, the continual evolution of cyber-attacks requires ongoing research and development of more robust and adaptive control strategies to ensure the integrity and stability of these critical systems.

Recent advances in LFC for power systems have increasingly focused on addressing the challenges posed by communication delays and cyber-attacks. Studies have explored various control strategies, each with unique approaches to mitigating these issues. For example, PIDD2 controllers have been designed for dual area thermal systems with delays up to 3.5 seconds [9], while PI controllers based on the maximum exponential decay rate (EDR) have been adapted for multi-area wind power systems, accommodating delays between 1 to 3 seconds [25]. Additionally, fault-tolerant event-triggered strategies have been reported using $H\infty$ control, with delay limits as low as 0.2 seconds [26]. In more complex scenarios, decentralized $H\infty$ control strategies have been proposed for network power systems, using probability models of delay representation under random attacks and varying delays [27]. Furthermore, PIDA controllers, optimized through supply-demand algorithms, have been applied to interconnected thermal power systems with time delays and attack scenarios [28]. Although these studies demonstrate significant progress, a complete understanding of the simultaneous impact of various attacks such as DoS and FDI, along with communication delays, remains a pressing challenge in the field [15], [16], [23], [29]. Many existing LFC methods focus primarily on minimal delays and often do not account for inherent delays during controller design [2], [4], [6]. Furthermore, only a limited number of strategies effectively incorporate both cyber-attacks and communication delays in their design [2], [6], [23], [27], limiting their applicability in addressing the complexities of real-world power system operations.

The objectives of this study are as follows.

- Extend the robust frequency-shifted internal model control (FIMC) method, previously used in chemical process control [30], to nonidentical dual area power systems with inherent delay and attacks.
- Apply the Golden Jackal Optimizer (GJO) [31] to determine the optimal value of the FIMC adjustment parameter (ψ) within the analytically determined range without relying on the hit-and-trial approach.
- Combine the merits of the metaheuristic GJO with the analytical FIMC to effectively manage cyber-attacks and communication delays in LFC.

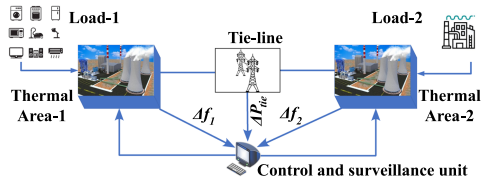

Fig. 1. Dual-area thermal power system as a CPS.

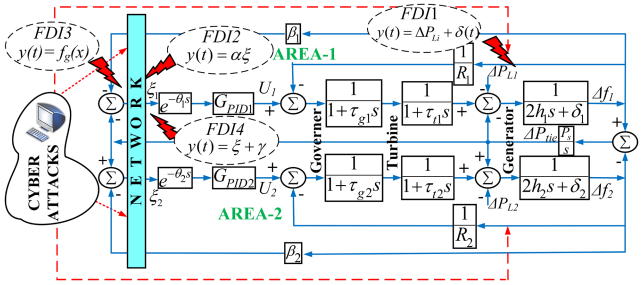

Fig. 2. Block diagram of non-identical dual-area non-reheated CPS.

This work contributes to the field in the following ways:

- Redesigns PID controllers for a dual-area thermal power system (both with and without delay) using the FIMC approach, obtaining a stable operating range of ψ via Routh stability analysis.
- Finds an optimal value of ψ within the stable operating range using GJO, treating the minimal integrated time square error (ITSE) as the objective function. This ψ serves as the only parameter for the FIMC-based PID design that determines the performance and robustness of the design.
- Model various false data injection (FDI) type cyber-attacks and communication delay to illustrate the robustness of the GJO-tuned FIMC controller in handling real-time uncertainties.

In Section II, test system is discussed together with detailed cyber-attacks. Section III discusses the controller design steps combined with the stability criteria for the chosen power system (PS) model with the proposed GJO algorithm. Section IV contains simulation and hardware-in-loop (HIL) validation performance. The final remarks are covered in Section V.

II. Theoretical Formulations

A. System Modeling

The model under consideration, depicted in Fig. 1, represents a thermal power plant with interconnected thermal areas (subscript $i \in \{1$: for area-1, 2: for area-2$\}$), operating without reheat and with nonidentical parameters. Each area has a base power rating of 1000 MVA and operates at a nominal frequency of 60 Hz. The synchronizing power coefficient, calculated using initial operating conditions, is found to be $P_s = 2.0$ per unit (pu) [32]. Each area is equipped with transfer functions of internal operating units such as speed governors ($G_{gi}(s)$) with non-reheated steam turbines ($G_{ti}(s)$) and generator units ($G_{gen,i}(s)$), as shown in Fig. 2 [32]. These transfer functions for the i_{th} area can be represented as

$$G_{gi}(s) = \frac{1}{1+\tau_{gi}s}; \quad G_{ti}(s) = \frac{1}{1+\tau_{ti}s}$$
$$G_{gen,i}(s) = \frac{1}{2h_i s+\delta_i} \tag{1}$$

In Fig. 2 $\beta_i \in \{\beta_1, \beta_2\}$ denotes the frequency bias parameters, $\xi_i \in \{\xi_1, \xi_2\}$ represents the area control errors (ACE), $r_i \in \{r_1, r_2\}$ denotes the speed-regulation constants, $\tau_{gi} \in \{\tau_{g1}, \tau_{g2}\}$, and $\tau_{gi} \in \{\tau_{t1}, \tau_{t2}\}$ denote the time constants of the governors and turbines of respective control areas. $\delta_i \in \{\delta_1, \delta_2\}$ is the frequency sensing load coefficients, while $h_i \in \{h_1, h_2\}$ represents inertia constant of the generation units of the respective areas. As $\beta_i = D_i + 1/R_i$, β_i [32], the closed-loop servo transfer function $G_{si}(s)$ of the ith-area plant without droop characteristics can be represented as,

$$G_{si}(s) = \beta_i \frac{G_{gi}(s)G_{ti}(s)G_{gen,i}(s)}{1 + G_{gi}(s)G_{ti}(s)G_{gen,i}(s)/r_i} \tag{2}$$

and can be represented by a third-order transfer function as

$$G_{si}(s) = \frac{\beta_i/A_i}{s^3 + (B_i/A_i)s^2 + (C_i/A_i)s + (D_i/A_i)} \tag{3}$$

where the variables $A_i = 2H_i\tau_{gi}\tau_{ti}$, $B_i = 2H_i\tau_{gi} + 2h_i\tau_{ti} + \delta_i\tau_{ti}\tau_{gi}$, $C_i = 2h_i + \delta_i\tau_{ti} + \delta_i\tau_{gi}$, and $D_i = \delta_i + 1/r_i$ can be evaluated for the respective areas. If IMC or FIMC-based controller design is carried out using the third-order model presented in (3), the numerator of the IMC or FIMC filter is also third order [30], [33]. In contrast, if the model in (3) can be simplified to a second-order model, by preserving the dominant poles of the full-order plant model and discarding the non-dominant poles, the usage of comparatively simpler controllers becomes feasible [34]. The Pade-based model reduction strategy employed in this study is based on matching a limited number of Taylor series expansion coefficients (c_{ki}) around $s = 0$ between the reduced order model and the original model [35]. Considering $g_{si}(t)$ being the impulse response of a high-order asymptotically stable system, the reduced order transfer function of the plant can be reconstructed as

$$G_{si}(s) = \int_0^\infty g_{si}(t)e^{-st}dt = c_{0i} + c_{1i}s + c_{2i}s^2 + \cdots$$
$$c_{ki} = \frac{(-1)^k}{k!}\int_0^\infty t^k g_{si}(t)dt, \; k = 0, 1, 2, \cdots \tag{4}$$

Using (3) and (4), $c_{0i}, c_{1i}, c_{2i}, c_{3i}, \cdots$ can be obtained as

$$c_{0i} = G_{si}(0)(-1)^0 = \frac{\beta_i}{D_i}, \; c_{1i} = G'_{si}(0)(-1)^1 = -\frac{C_i\beta_i}{D_i^2}$$
$$c_{2i} = \frac{G''_{si}(0)(-1)^2}{2!} = \frac{2\beta_i C_i^2}{D_i^3} - \frac{2B_{\beta_i}}{D_i^2}$$
$$c_{3i} = \frac{G'''_{si}(0)(-1)^3}{3!} = \frac{12B_i\beta_i C_i}{D_i^3} - \frac{6\beta_i C_i^3}{D_i^4} - \frac{6A_i\beta_i}{D_i^2}$$
$$\cdots \tag{5}$$

For an i_{th} area, let the reduced-order model $G_{si}(s)$ can be defined as

$$G_{si}(s) = \frac{a_{0i} + a_{1i}s + a_{2i}s^2 + \cdots + a_{(k-1)i}s^{k-1}}{b_{0i} + b_{1i}s + b_{2i}s^2 + \cdots + b_{(k-1)i}s^{k-1} + s^k} \quad (6)$$

where $a_{0i}, a_{1i}, \ldots, a_{(k-1)i}$ and $b_{0i}, b_{1i}, \ldots, b_{(k-1)i}$ are the coefficients in numerator and denominator of the reduced-order model $G_{si}(s)$, respectively. For $G_{si}(s)$ in (6) to be a Pade-approximated version of $G_{si}(s)$ in (4), the following conditions must be met [35]:

$$\begin{aligned} &a_{0i} = b_{0i}c_{0i}, \quad a_{1i} = b_{0i}c_{1i} + b_{1i}c_{0i} \\ &\cdots \end{aligned} \quad (7)$$

Using (6) and (7), a second-order reduced model $G_{si}(s)$ for $k = 0, 1$ can be obtained as

$$G_{si}(s) = \frac{a_{0i} - a_{1i}s}{b_{0i} + b_{1i}s + s^2} \quad (8)$$

Here, the coefficients a_{0i}, a_{1i}, b_{0i} and b_{1i} can be evaluated by substituting c_{0i}, c_{1i}, c_{2i} and c_{3i} from (5) in (9).

$$\begin{aligned} -c_{0i} &= c_{2i}b_{0i} + c_{1i}b_{1i}; \quad a_{0i} = c_{0i}b_{0i} \\ -c_{1i} &= c_{3i}b_{0i} + c_{2i}b_{1i}; \quad -a_{1i} = c_{1i}b_{0i} + c_{0i}b_{1i} \end{aligned} \quad (9)$$

Given that LFC primarily addresses the disturbance mitigation issue, the goal is to stabilize the system G_{si} amid demand fluctuations (ΔP_{Li}), simultaneously diminishing the impact of ΔP_{Li} on frequency changes Δf_i via control actions. From Fig. 2, the frequency deviation Δf_i can be observed as

$$\Delta f_i(s) = G_{si}(s)U_i(s) + G_{Di}(s)\Delta P_{Li}(s) \quad (10)$$

where U_i is the controller output. G_{Di} is the regulatory transfer functions. The relation between ξ_i, ΔP_{tie} (tie-line power deviation) and Δf_i can be obtained from Fig. 2 as

$$\xi_i = \beta_i \Delta f_i + \Delta P_{tie} \quad (11)$$

The ACE signal is produced by keeping track of the frequency and tie-line power variations, which serve as input to the controller.

B. Cyber-Attacks

The crucial role in automatic generation control for information-based power transfer is played by the propagation of accurate measurements, specifically Δf_i and ΔP_{tie}, obtained from the sensor or feedback channel. These measurements are vital as they are processed to compute the ACE, which in turn affects the control signal sent to the actuator or process plant. Unfortunately, these measurements can be manipulated, leading to control actions that could significantly compromise the operation of the actual power plant and result in unstable and uneconomically transferred power within interconnected systems. Attackers, leveraging remote access, can infiltrate the open communication channel's vulnerability arising from large-scale operations, and introduce an attack signal that corrupts incoming measurements, namely Δf_i and ΔP_{tie} [19]. In the attack models discussed in this article, the manipulated measurements Δf_i and ΔP_{tie} are injected with the intent of falsifying the actual ACE measurements, as ACE plays a crucial role in the smooth exchange of tie-line power and uniform frequency maintenance.

To illustrate various types of attacks, the model shown in Fig. 2 is treated as a CPS, incorporating sensing, communication, and computer technology. Points of vulnerability where attackers can gain access are highlighted with arrows in Fig. 2. This study aims to validate the robustness of the FIMC controller against such unforeseen scenarios and to demonstrate its innate ability to handle unexpected disturbances. Various attack models are considered for this purpose, based on the models discussed in [16]. Some of these models are elaborated below:

1) Location Attack: This is an attack that can be channeled through the load disturbance input point ΔP^*_{Li}. The attacker drops the manipulated data through the point of load disturbance ΔP_{Li} for a particular period when there is no active load disturbance. The mathematical equation of the attack input superimposed on the load disturbance is as follows [16]:

$$\Delta P^*_{Li} = \begin{cases} \Delta P_{Li} & \forall\, t = t_1 \\ \Delta P_{Li} + \lambda(t) & \forall\, t \in \tau_a;\ t_2 < \tau_a < t_3 \end{cases} \quad (12)$$

where ΔP^*_{Li} is the load disturbance at step time $t = t_1$. $\lambda(t) = r * (u(t - t_2) - u(t - t_3))$ (where $r = a + (b - a) * rand(N, 1)$) is the input for the attack that is a product of a uniform random number r (with lower limit a and upper limit b) and the input for the step for the duration of the attack τ_a. Note that the $rand$ command is used to generate uniform random numbers for a given attack span. The smooth control operation of interconnected areas is hindered during the attack period, and consequently the power quality at the receiving end (grid and substations) is seriously compromised, resulting in unevenly fluctuating dynamic response.

2) Scaling Attack: This is a type of template attack that results in the alteration of ACE amplitude by scaling the Δf_i and ΔP_{tie}. Accordingly, ACE is either decreased or incremented. The modified ACE after attack ξ^*_u is mathematically expressed as follows [16]:

$$\xi^*_u = \begin{cases} \alpha(\beta_i \Delta f_i + \Delta P_{tie}) & \forall\, t \in \tau_a \\ \beta_i \Delta f_i + \Delta P_{tie} & \forall\, t \notin \tau_a \end{cases} \quad (13)$$

where α is the error scaling factor and τ_a is the duration of the attack. Other symbols have their usual meanings, as stated in (11). Due to the scaling attack, the magnitude of the ACE is falsified for the duration of the attack, leading to the transmission of the corrupted control input to the plant, resulting in an uneven deviation in the operating frequency.

3) Random Attack: In this type of attack, false and random error inputs are sent through the channel present at the attack point. This initiates the control action when there is no actual error. It is also a type of scaling attack, except for the fact that the ACE input is scaled by a certain degree of randomness. The signals transmitted through the communication channel go completely in haywire mode, deteriorating dynamic performance. The value of ACE after the attack ξ^*_u is mathematically expressed as follows [16]:

$$\xi^*_u = \begin{cases} \frac{1}{\sigma\sqrt{2\pi}} e^{\frac{-(x-\mu)^2}{2\sigma^2}} \rightarrow f_g(x) & \forall t \in \tau_a \\ \beta_i \Delta f_i + \Delta P_{tie} & \forall t \notin \tau_a \end{cases} \quad (14)$$

During attack execution, the normal incoming feedback input through the ACE channel is blocked and input $f_g(x)$ is dropped. Here, μ is the mean of the distribution, σ is the standard deviation, and τ_a is the duration of the attack. Other symbols have their usual meanings, as stated in (11). Also, the signal $f_g(x)$ is Gaussian in nature and is fed through the channel to the controller, which in turn generates arbitrary control commands that cause fluctuation in f_i and P_{tie}.

4) Data Integrity Attack: The transmission channel is manipulated by injecting a false data input, which, in turn, falsifies the actual ACE fed to the controller. Thus, the modified ACE input becomes ξ_u^*, which is as follows [16]:

$$\xi_u^* = \begin{cases} \beta_i \Delta f_i + \Delta P_{tie} + \gamma & \forall\, t \in \tau_a \\ \beta_i \Delta f_i + \Delta P_{tie} & \forall\, t \notin \tau_a \end{cases} \tag{15}$$

where γ denotes the false signal used to corrupt the measurements to affect the integrity of operation. Other symbols have their usual meanings, as stated in (11). Being a type of FDI attack, it is capable of corrupting the real-time ACE data in LFC systems, which in turn disrupts real-time maintenance of operating frequency. The relevant simulation results concerning cyber-attacks are presented in Section IV.

5) Resonance Attack: The system is attacked with an input signal $Asgn(y_1(t-\phi))$ such that the load demand is altered as follows

$$\begin{aligned} \Delta P_{Li}^* &= \Delta P_{Li} - x_f \,\mathrm{sgn}(y_f(t-\phi)) \\ &= \begin{cases} \Delta P_{Li} - x_f; & y_f(t-\phi) > 0 \\ \Delta P_{Li} + x_f; & y_f(t-\phi) \le 0 \end{cases} \end{aligned} \tag{16}$$

In the above equation, x_f is the required rate of change of frequency (RoCoF), y_f is a sinusoidal function with a phase lag of ϕ. Consequently, the attacked power plant will be disconnected from the entire power system, as the RoCoF relays will continue to tripped due to the manipulated measurements, which can cause a shortage of power supply and overload of other interconnected areas.

Remark 1: Disturbances tend to cause the controlled variable (frequency deviation) to deviate from the zero set point. In contrast, FDIA corrupts the measurements of ΔF_1 and ΔF_2 with false data. This eventually causes a blackout if not addressed. The models of disturbances and FDIA used in this work are also different. As discussed in Section IV, step and random load disturbances are considered. In contrast, the FDIA models belong to location, data integrity and resonance types.

III. Proposed FIMC With Optimized Coefficients

The block diagrammatic structure outlined in Fig. 3 is a basic plant-level control for ith area CPS presented in Fig. 2. Here, $G_i(s)$ is the plant transfer function with the internal model $G_{si}(s)$ that is factored into invertible parts $G_{si-}(s)$ and non-invertible $G_{si+}(s)$ parts. Generally, $E(s)$ and $R(s)$ denote the error and reference, respectively. In the context of the CPS considered in Fig. 2, $E(s)$ refers to the ACE while $R(s)$ indicates the reference value (zero) that must be followed by the controlled variable (Δf_i). $G_{Di}(s)$ be disturbance transfer function. In this

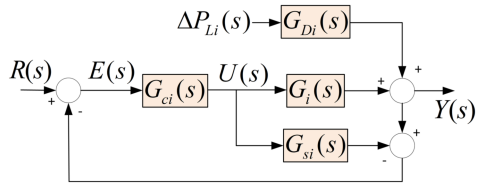

Fig. 3. Proposed FIMC structure.

work, the disturbance transfer function is taken the same as that of the generator transfer function as the load perturbation ΔP_{Li} appears at the generator input in Fig. 2. According to the block diagram reduction principle, $G_i(s)$ of Fig. 3 indicates $G_{gen,i}(s)$ in Fig. 2. $D(s)$ indicates the random/step load disturbance. Taking $G_{ci}(s)$ as the controller transfer function, the IMC controller [35] is obtained as follows:

$$G_{ci}(s) = G_{fi}(s)\frac{1}{G_{si-}(s)}; \quad G_{fi}(s) = \frac{1}{(ks+1)^n} \tag{17}$$

where the transfer function $G_{fi}(s)$ represents nth-order low-pass filter with a tuning parameter k to achieve a satisfactory closed-loop response. Conventional IMC-based PID controller designs are affected by an additional phase delay due to $G_{fi}(s)$, which requires the use of a FIMC strategy for improved performance and robustness. As such, the FIMC strategy becomes crucial when dealing with LFC problems amidst real-time challenges such as CDs, CAs, and parametric uncertainties, providing more sophisticated schemes to tune parameter selection. In the FIMC strategy, the controller $G_{ci}(s)$, is designed using a frequency-shifted version of the plant model, $G_{si}(s-\psi_i)$, instead of $G_{si}(s)$. This adjustment allows for an enhanced robustness of $G_{ci}(s)$ that can be varied by changing the variable $\psi_i \in \{\psi_1$: for area-1, ψ_2: for area-2$\}$, making the control loop less sensitive to parametric aberrations for $\psi_i < 0$, thus ensuring higher robustness [30].

A. Proposed FIMC-PID Design

The FIMC-PID design primarily aims at finding a stable operating range for ψ_i, which, when fed into the GJO, results in an optimal FIMC-PID controller that ensures an improved performance-robustness trade-off. Using the reduced order model (8), the pole-zero frequency-shifted version of plant internal model $G_{si}(s)$, i.e., $G_{si}(s-\psi_i)$ can be obtained as

$$\begin{aligned} G_{si}(s-\psi_i) &= \frac{a_{0i} - a_{1i}(s-\psi_i)}{b_{0i} + b_{1i}(s-\psi_i) + (s-\psi_i)^2} \\ &= G_{si-}(s-\psi_i) G_{si+}(s-\psi_i) \end{aligned} \tag{18}$$

where the invertible and non-invertible components are

$$\begin{aligned} G_{si-}(s-\psi_i) &= \frac{a_{0i} + a_{1i}\psi_i + a_{1i}s}{b_{0i} + b_{1i}(s-\psi_i) + (s-\psi_i)^2} \\ G_{si+}(s-\psi_i) &= \frac{a_{0i} + a_{1i}\psi_i - a_{1i}s}{a_{0i} + a_{1i}\psi_i + a_{1i}s} \end{aligned} \tag{19}$$

TABLE I
OPTIMAL CONTROLLER SETTINGS FOR FIMC-PID

Optimizers	Controller Settings					
	Area-1			Area-2		
	K_{pi}	K_{di}	K_{ii}	K_{pi}	K_{di}	K_{ii}
AO	2.473	0.97	4.718	1.486	0.87	3.037
EO	2.252	0.97	4.449	1.513	0.87	3.061
AVOA	2.467	0.97	4.709	1.472	0.87	3.025
PSO	1.303	0.97	3.58	0.849	0.87	2.61
GJO	2.313	0.97	4.520	1.524	0.87	3.069

The idealized FIMC controller can be represented as

$$G_{ci}(s) = \frac{1}{G_{si-}(s-\psi_i)} = \frac{b_{0i} + b_{1i}(s-\psi_i) + (s-\psi_i)^2}{a_{0i} + a_{1i}\psi_i + a_{1i}s} \tag{20}$$

The expression for the FIMC-PID controller transfer function for the i_{th} area can be obtained as

$$G_{PIDi}(s) = \frac{G_{ci}(s)}{1 - G_{ci}(s)G_{si}(s-\psi_i)} = \frac{s^2 + (b_{1i} - 2\psi_i)s + b_{0i} - b_{1i}\psi_i + \psi_i^2}{2a_{1i}s} \tag{21}$$

By comparing the coefficients of (21) with the ideal PID controller transfer function $K_{pi} + K_{ii}/s + K_{di}s$, it is possible to obtain the following:

$$K_{pi} = \frac{b_{1i} - 2\psi_i}{2a_{1i}}; \quad K_{ii} = \frac{\psi_i^2 - b_{1i}\psi_i + b_{0i}}{2a_{1i}}; \quad K_{di} = \frac{1}{2a_{1i}} \tag{22}$$

The FIMC-PID controller gains are optimized using various algorithms, including the AO, EO [5], AVOA, PSO [2], and the GJO are detailed in Table I. The primary limitation of PSO lies in its tendency to get trapped in local optima in cases of diverse search spaces [36]. To circumvent this limitation, various mutation schemes have been proposed [37]. However, it is important to note that the incorporation of such schemes extends beyond the scope of our current work. In our study, we have adhered to the standard PSO parameters as established in [38], which includes setting $w_1 = c_1 = c_2 = 0.5$. This choice was made to maintain a baseline comparison with the original PSO algorithm, without introducing additional complexities through mutation or other enhancement strategies. Therefore, the distinct gains of PSO observed in Table I is a consequence of its native algorithmic behavior under the given settings, rather than a direct relation to the selection of ITSE for multi-objective functions. The stability margins of the FIMC-PID settings obtained by different algorithms and their corresponding computation times are compared in Table II. From this table, it is evident that the GJO-tuned FIMC-PID settings yield better stability margins with lesser computation time compared to EO, AO and PSO.

The dynamic response comparison of FIMC-PID tuned with different algorithms are presented in Fig. 4. Though the computation time of GJO is slightly higher than that of AVOA, the latter results in an oscillatory dynamic response as evident in Fig. 4. The settling time (T_s), overshoot (MOS), and undershoot (MUS) of various algorithms are presented in Table III in addition to the figure of demerit (FOD). Here, GJO shows the

TABLE II
COMPUTATIONAL TIME AND STABILITY MARGINS FROM OPTIMIZERS

Optimizers	T_{com} (sec)	Area-1		Area-2	
		GM (dB)	PM (deg)	GM (dB)	PM (deg)
AO	114.82	14	9.38	-22.4	3.1
EO	120.39	24.7	19.7	-1.59	-1.53
AVOA	66.52	22.3	22.6	9.54	-3.72
PSO	140.27	9.58	-18.3	28.9	40.2
GJO	68.05	19.9	27.3	11.7	16.0

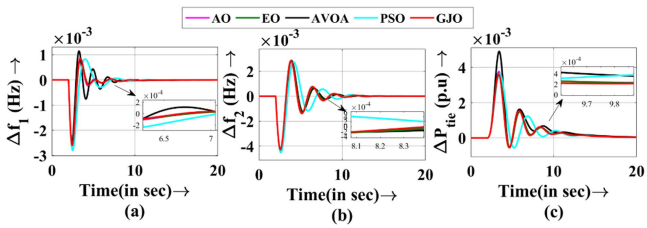

Fig. 4. Plots of dynamic responses with different optimizers: (a) Deflection in frequency for area-1, (b) Deflection in frequency for area-2, and (c) Deflection in tie-line power.

TABLE III
COMPARISON OF DIFFERENT OPTIMIZERS

Algo.	Area-1 (Δf_1)			Area-2 (Δf_2)			ΔP_{tie}			FOD
	T_s (s)	MOS (mHz)	MUS (mHz)	T_s (s)	MOS (mHz)	MUS (mHz)	T_s (s)	MOS (mpu)	MUS (mpu)	$\times 10^{-3}$
AO	8.41	8.65	-0.26	9.62	2.8	-4.2	14.66	0.38	-5.45	21.0
EO	6.49	8.28	-0.26	9.66	2.8	-4.2	14.69	0.36	-5.19	21.0
AVOA	7.93	11.43	-0.25	9.87	2.9	-4.3	14.82	0.49	-5.45	21.6
PSO	8.08	8.27	-0.28	11.53	2.7	-4.5	14.76	0.36	-5.63	27.6
GJO	8.42	8.57	-0.25	9.54	2.8	-4.2	14.56	0.35	-5.51	20.9

best fitness value after 10 iterations, demonstrating better convergence characteristics during the dynamic response to a 10% step load disturbance (SLD) at $t = 2$ s. This robust performance of GJO can be attributed to its foundation as a nature-inspired optimization technique that emulates the hunting pattern of a golden jackal [31].

Subsequently, the FIMC-PID controller gains are tuned with the GJO by considering a Multi-Objective Function (MOF) incorporating Integrated Squared Error (ISE), Integrated Absolute Error (IAE), and Integrated Time-weighted Absolute Error (ITAE). However, the Integrated Time Square Error (ITSE) is chosen due to its superior dynamic response characteristics with minimal overshoot, undershoot and settling times, as shown in Fig. 5. Therefore, GJO is adopted to identify the optimal values of ψ_i for each control area with the objective of minimizing the ITSE function provided in (23).

$$J_{ITSE} = \int_0^T (\xi_1^2 + \xi_2^2) t dt \tag{23}$$

where ξ_1 and ξ_2 are ACEs in area-1 and area-2, respectively. T is the simulation time chosen to demonstrate transient and steady-state responses. ITSE criteria uses the time multiplication term to drastically penalize the error as time progresses. Therefore, it

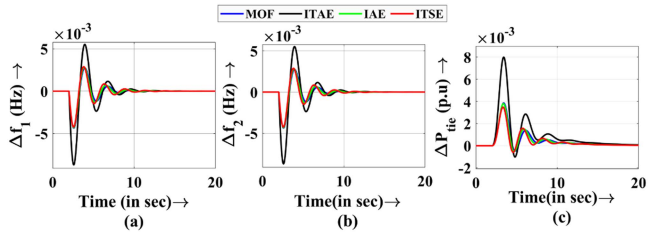

Fig. 5. Plots of dynamic responses with different objective functions: (a) deflection in frequency for area-1, (b) deflection in frequency for area-2, and (c) deflection in tie-line power.

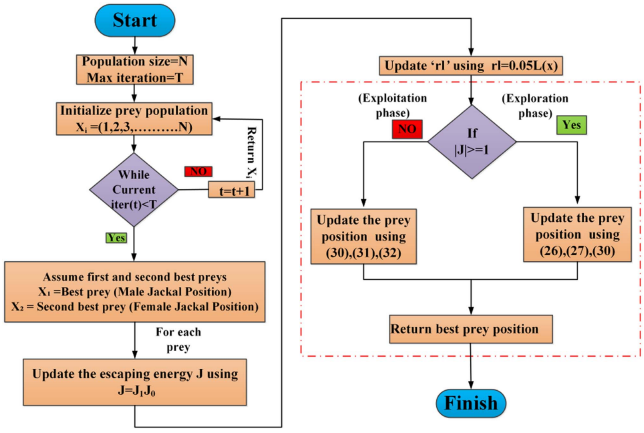

Fig. 6. Flowchart of the proposed GJO.

effectively reduces the settling time, which cannot be achieved with ITAE, IAE or ISE based tuning [39].

B. Golden Jackal Optimizer

GJO is a nature-inspired optimization technique [31] that mathematically replicates the hunting pattern of a golden jackal. GJO has been reported to have better fitness characteristics compared to its predecessors, such as PSO [2], AVOA, AO and EO [5]. Therefore, this algorithm has been adopted to obtain the appropriate values of ψ for each control area so that ITSE is minimized. The three main steps of GJO are searching for prey, exploration, and exploitation (enclosing and pouncing the prey), which are summarized in the flow chart of Fig. 6 and explained as follows:

1) Search Periphery Modeling Phase: Since GJO uses a population-oriented strategy, it is assumed that the initial solution is evenly distributed throughout the search range. Therefore, in the first test, we assume the following:

$$X_0 = X_{\min} + rand\,(X_{\max} - X_{\min}) \tag{24}$$

where '$rand$' is a uniform random vector with a value between 0 and 1. $X_{\min}$ and $X_{\max}$ are the lower and upper limits of the variables, respectively. This initialization generates the initial prey matrix, with the jackal pair ranking first and second best. The prey matrix is as follows:

$$prey = \begin{pmatrix} X_{1,1} & X_{1,2} & \cdots & X_{1,d} \\ X_{2,1} & X_{2,2} & \cdots & X_{2,d} \\ \vdots & \vdots & \ddots & \vdots \\ X_{n,1} & X_{n,2} & \cdots & X_{n,d} \end{pmatrix} \tag{25}$$

X_{ij} stands for the i_{th} prey's j_{th} dimension. In this case, n stands for the number of prey and d stands for the number of variables. There is a distinct solution for each position of the prey. Note that the corresponding prey locations are acquired by the jackal pair according to the fitness value imparted to each prey for the next phase called exploration.

2) Exploration Phase: Because of their nature, jackals are skilled in spotting and chasing prey. Sometimes, the prey escapes and escapes. Usually, jackals use the wait-and-watch method in such a scenario. Male jackals lead the hunting, while female jackals follow them. This strategy is mathematically expressed as follows.

$$X_1(t) = X_M(t) - J.\,|X_M(t) - rl.prey(t)| \tag{26}$$

$$X_2(t) = X_{FM}(t) - J.\,|X_{FM}(t) - rl.prey(t)| \tag{27}$$

where t indicates the present iteration. '$prey(t)$' indicates the position vector of the prey. $X_M(t)$ and $X_{FM}(t)$ denote the positions of the male and female jackals, respectively. Additionally, $X_1(t)$ and $X_2(t)$ are the revised positions of the male and female jackals. Escaping energy of the prey is calculated as $J = J_1 J_0$ [31], where J_1 indicates the declining energy of the prey and $J_0 = (2r - 1)$ indicates the initial energy of the prey. Here, r is a random number between 0 and 1.

$$J_1 = A_1\,(1 - (t/T)) \tag{28}$$

where $A_1 = 1.5\,T$ denotes the best possible number of iterations with the present iteration t. After some iterations, J_1 gradually decreases from 1.5 to 0. $|rl.prey(t)|$ (in (26)–(27)) indicates the distance between the jackal and the prey. This distance is added and subtracted, and this is mainly attributed to the escaping energy of the prey. Furthermore, (rl =0.05$L(x)$), is a vector of random numbers based on the levy distribution [31] with L as the levy flight function that can be computed as

$$L(x) = 0.01(\mu\sigma)(|v^{(1/\beta)}|),\ \sigma = \left(\frac{\Gamma\,(1+\beta)\sin\left(\frac{\pi\beta}{2}\right)}{\Gamma\left(\frac{1+\beta}{2}\right)\beta\left(2^{\frac{\beta-1}{2}}\right)}\right)^{\frac{1}{\beta}} \tag{29}$$

where u and v are random variables in the range (0, 1) and $\beta = 1.5$. Finally, the jackal positions are revised taking the mean of (26) and (27) as follows:

$$X(t+1) = \frac{X_1(t) + X_2(t)}{2} \tag{30}$$

3) Exploitation Phase: At this point, the ability of the prey to evade the jackal's pursuit begins to wane, and the jackal pair encloses the prey, as discussed in the previous stage. As a result, they attack the prey and consume it. The following

mathematical model describes the attack pattern of both male and female jackals.

$$X_1(t) = X_M(t) - J.\,|rl.X_M(t) - prey(t)| \tag{31}$$

$$X_2(t) = X_{FM}(t) - J.\,|rl.X_{FM}(t) - prey(t)| \tag{32}$$

where t indicates the present iteration. prey(t) is the position vector of the prey. $X_M(t)$ and $X_{FM}(t)$ denote the positions of the male and female jackals, respectively. Furthermore, the revised positions of male and female jackals that correlate with prey are $X_1(t)$ and $X_2(t)$. Also, the escaping energy J is computed. The function rl used in (31) and (32) is utilized to impart arbitrary behavior in the exploitation phase, thus favoring exploration. The energy escaping is essentially employed as a basis for going from exploration to exploitation. Throughout the escape behavior of the prey, its energy continues to decrease significantly. In general, jackal couples analyze various areas for prey, thereby escaping energy, i.e., $|J| > 1$. When $|J| < 1$, jackal pairs attack the prey and carry out the exploitation.

C. Comparison of IMC and FIMC on Grounds of Maximum Sensitivity

For the IMC approach [35] the PID controller parameters are obtained for the plant model given in (3) as $K_{i1} = (2k_1 + 0.139)^{-1}$, $K_{p1} = 0.363K_{i1}$, and $K_{d1} = 0.271K_{i1}$ for area-1 and $K_{i2} = 1.002(2k_2 + 0.192)^{-1}$, $K_{p2} = 0.326K_{i2}$, and $K_{di} = 0.334K_{i2}$ for area-2, respectively. Maximum sensitivity (M_S), which is a marker of the degree of robustness [30] can be represented as

$$M_S = \max\left|\frac{1}{1+L(s)}\right| \in [1.2,\ 2],\ \text{for stable operation} \tag{33}$$

where $L(s) \to L(j\omega)$ denotes the product of the controller and plant transfer function. By substituting the parameters of the power system in (22), the FIMC controller coefficients can be obtained as

For Area-1:

$$K_{p1} = \frac{1.342 - 2\psi_1}{1.03};\ K_{i1} = \frac{\psi_1^2 - 1.342\psi_1 + 3.687}{1.03};\ K_{d1} = 0.970$$

For Area-2:

$$K_{p2} = \frac{0.976 - 2\psi_2}{1.149};\ K_{i2} = \frac{\psi_2^2 - 0.976\psi_2 + 2.999}{1.149};\ K_{d2} = 0.870$$

For a fair comparison, the level of robustness has to be kept the same for both FIMC and IMC controllers. To demonstrate this, both the IMC and the FIMC strategies are designed for $M_S = 1.4$ (without tuning the respective tuning parameters with GJO). The respective tunable parameter (i.e ψ_i for FIMC and K_{ii} for IMC) corresponding to $M_S = 1.4$ is traced from the M_S vs. K_{ii} plot for the IMC in Fig. 7(a) and the M_S vs. ψ_i plot for the FIMC in Fig. 7(b) for each area. Subsequently, these chosen tuning parameters are used to obtain the controller settings for each area. From the results shown in Fig. 8, it can be perceived that the FIMC control strategy gives better performance compared to IMC given the same level of robustness.

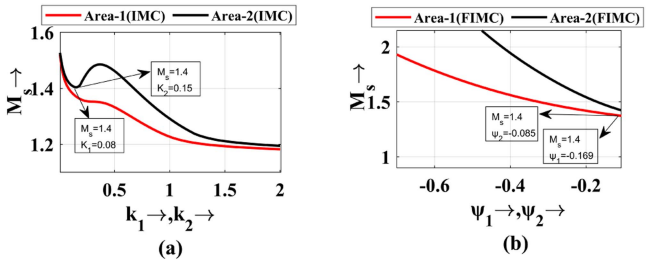

Fig. 7. M_S Vs tuning parameter curve for (a) IMC and (b) FIMC.

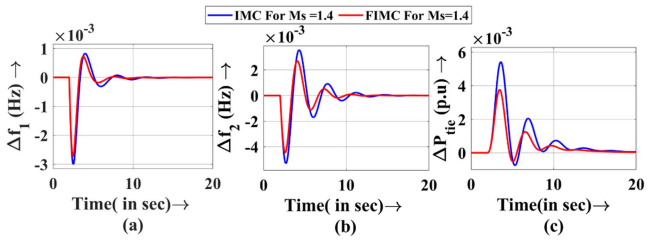

Fig. 8. Fair comparison on same degree of robustness $M_S = 1.4$. (a) Deflection in frequency for area-1. (b) Deflection in frequency for area-2. (c) Deflection in tie-line power.

D. Obtaining a Stable Empirical Range of ψ_i

Since the PID coefficients given in (22) are dependent on ψ_i, it is essential to establish a stable analytical range for ψ_i in both areas. This can be achieved by employing the Routh-Hurwitz (RH) stability criteria. Therefore, by utilizing (3) and (22), the closed-loop characteristic equation can be formulated as

$$1 + G_{si}(s)G_{PIDi}(s) = 0 \tag{34}$$

Rearranging (3), (22), and (34), a polynomial is obtained in (35).

$$A_i s^4 + B_i s^3 + (\beta_i K_{di} + C_i)s^2 + (\beta_i K_{pi} + D_i)s + \beta_i K_{ii} = 0 \tag{35}$$

The following inequalities are obtained by using RH conditions for stability:

$$\begin{gathered} \beta_i K_{ii} > 0 \\ B_i\beta_i K_{di} + B_i C_i - A_i\beta_i K_{pi} - A_i D_i > 0 \\ \begin{pmatrix} B_i C_i D_i + K_{pi} B_i C_i \beta_i + B_i D_i \beta_i K_{di} + K_{pi} B_i \beta_i^2 K_{di} \\ -A_i(\beta_i^2 {K_{pi}}^2 + D_i^2 + 2\beta_i K_{pi} D_i) - B_i^2 \beta_i K_{ii} \end{pmatrix} > 0 \end{gathered} \tag{36}$$

where the expressions of A_i, B_i, C_i, and D_i are given below of (3) for ith-area. Substituting the system parameters into (36) yields ψ_i, i.e., $-2.109 < \psi_1 < 0.778$ and $-1.385 < \psi_2 < 0.57$. It should be noted that the above range of ψ_1 and ψ_2 are obtained without considering delay.

E. Controller Design Amid Communication Delay

For designing the FIMC-PID controller in the presence of CD, a delay term is considered in (8) as follows:

$$G_{si\theta}(s) = G_{si}(s)e^{-\theta s} = \frac{a_{0i}\left(1 - \frac{a_{1i}}{a_{0i}}s\right)e^{-\theta s}}{b_{0i} + b_{1i}s + s^2} \tag{37}$$

The numerator term $1-(a_{1i}/a_{0i})s$ of (37) is approximated as a delay term $e^{(-a_{1i}/a_{0i})s}=1-(a_{1i}/a_{0i})s$ using the Taylor series approximation to get

$$G_{si\theta}(s)=\frac{a_{0i}e^{-\theta s}e^{-\left(\frac{a_{1i}}{a_{0i}}\right)s}}{b_{0i}+b_{1i}s+s^2} \tag{38}$$

Using the FIMC-PID design approach elucidated in Section II-I-B, we get the following settings:

$$K_{pi}=K_{di}\left(b_{1i}-2\psi_i\right),\quad K_{ii}=K_{di}\left(\psi_i^2-b_{1i}\psi_i+b_{0i}\right)$$
$$K_{di}=\left(2a_{0i}\left(\theta+\tfrac{a_{1i}}{a_{0i}}\right)\right)^{-1} \tag{39}$$

The steps given in (34)–(36) are followed to obtain the stable range of ψ_i taking $G_{si}(s)$ with inherent delay θ as follows:

$$G_{si}(s)=\frac{\beta_i(1-\theta s)}{A_is^3+B_is^2+C_is+D_i} \tag{40}$$

To receive real-time control command signals without any time lag, a robust counter-delay control strategy is needed for effective LFC. In the two-area test system, an inherent communication delay of θ s is taken into account. For example, if $\theta=1$ s, the range of ψ_i obtained using Routh-Hurwitz analysis in both control areas is as follows: $-0.289<\psi_1<1.864$ (for area 1) and $-0.619<\psi_2<1.644$ (for area 2). For $\theta=3.5$ sec and using the power system parameters of [9], we get $-3.392<\psi_1<1.161$ (for area-1) and $-25.756<\psi_2<4.19$ (for area-2). The same procedure can also be extended for other values of delays and power system parameters.

F. Stability Analysis in the Frequency Domain

The generalized Laplace transform representation of the nominally controlled i_{th} area PS ([4]) is as follows:

$$\Delta f_i(s)=G_{si}(s)U_i(s)+G_{Di}(s)\Delta P_{Li}(s) \tag{41}$$

Substitution $\Delta P_{Li}(s)=0$ (perceiving LFC as a disturbance mitigation problem) in (2), we get

$$\frac{\Delta f_i(s)}{U_i(s)}=G_{si}(s) \tag{42}$$

For stability analysis, the Bode plot is obtained for area-1 and area-2 using the following transfer function:

$$G_{s1}(s)=\frac{20.6(1-s)}{s^3+7.06s^2+10.42\,s+20.6} \tag{43}$$

$$G_{s2}(s)=\frac{16.906(1-s)}{1.44s^3+7.3607s^2+8.81\,s+16.906} \tag{44}$$

It is revealed from Fig. 9 that the closed-loop configuration for both areas of the power system remains stable using the linear analysis toolbox palette in Simulink. Closed-loop stability is not compromised even in the presence of delay. With the GJO tuned FIMC-PID control strategy, stability is also ensured. The corresponding stability markers such as (gain margin >0, phase margin >0) in the frequency domain analysis are highlighted in the bode plot for area-1 and area-2, as shown in Fig. 9.

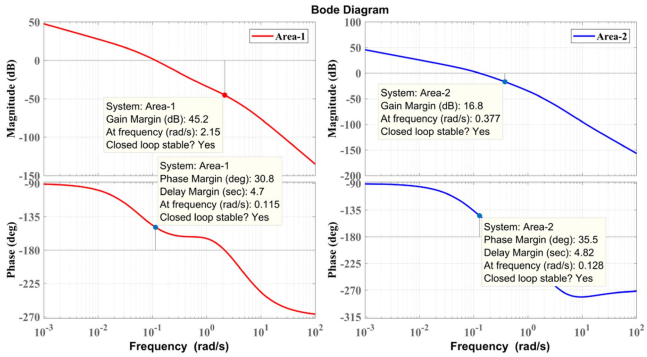

Fig. 9. Bode graph with stability margins.

TABLE IV
GJO-TUNED OPTIMIZED SETTINGS FOR CHOSEN CONTROL TECHNIQUES

Controller.	Gains	Area-1	Area-2	Controller.	Gains	Area-1	Area-2
FIMC-PID	K_p	2.313	1.524	PI	K_p	0.303	0.246
	K_i	4.520	3.069		K_i	0.587	0.226
	K_d	0.970	0.870		K_d	0	0
IMC-PID	K_p	0.163	0.122	I	K_p	0	0
	K_i	0.451	0.377		K_i	0.273	0.290
	K_d	0.122	0.125		K_d	0	0

IV. RESULTS AND DISCUSSIONS

The system mentioned in Fig. 2 is utilized to validate the proposed control method using MATLAB/Simulink-based simulations with the following parameter settings:

For area-1: $r_1=0.05$ Hz/pu MW, $\delta_1=0.6$, $h_1=5$ s, $\beta_1=20.6$ pu MW/Hz, base power $(P_b)=1000$ MVA, $\tau_{g1}=0.2$ s, $\tau_{t1}=0.5$ s.

For area-2: $r_2=0.0625$ Hz/pu MW, $\delta_2=0.9$, $h_2=4$ s, $\beta_2=16.9$ pu MW/Hz, $P_b=1000$ MVA, $\tau_{g2}=0.3$ s, $\tau_{t2}=0.6$ s.

During such a validation, a load disturbance of 0.1 pu is maintained in both interconnected areas. Initially, the performance of GJO-tuned controllers is compared with various existing works. In addition, the effect of cyber-attacks on the proposed work is also investigated in the following subsections. In the end, the proposed controller validation through HIL implementation is discussed. For the analysis carried out in Sections IV-A–IV-B, the aforementioned power system parameters adopted from [32] are used. For the subsequent studies presented in Sections IV-C–IV-E, the power system parameters of [9] is utilized for fair comparison:

For area-1: $R_1=0.05$ Hz/p.u.MW, $D_1=1$, $H_1=10$ s, $B_1=21$ p.uMW/Hz, Base power $=1000$MVA, $\tau_{g1}=0.1$ s, $\tau_{t1}=0.3$ s,

For area-2: $R_2=0.05$ Hz/p.u.MW, $D_2=1.5$, $H_2=12$ s, $B_2=21.5$ p.u.MW/Hz Base power $=1000$MVA, $\tau_{g2}=0.17$ s, $\tau_{t2}=0.4$ s.

A. Performance Comparison With GJO-Tuned Controllers

To demonstrate the dynamic behavior of various GJO-tuned controllers, an SLD of 10% or 0.1 pu (at $t=2$ s) is applied to both interconnected control areas. The GJO-tuned controller settings are given in Table IV. Dynamic responses are shown

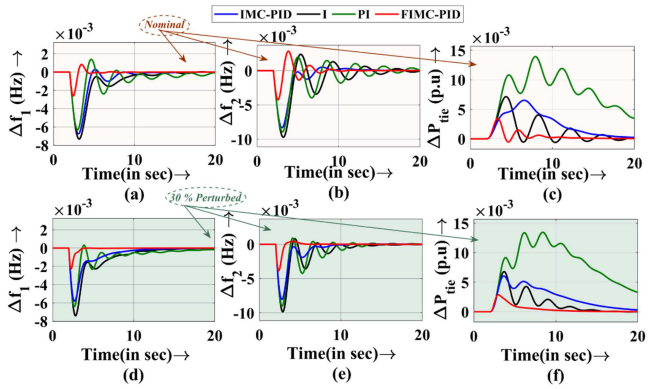

Fig. 10. Plots of dynamic responses with different controllers: under nominal conditions (a)–(c) and under 30% perturbed cases (d)–(e); (a), (d) frequency deflection in area-1; (b), (e) frequency deflection in area-2; and (c), (f) deflection in tie-line power.

TABLE V
COMPARISON OF DIFFERENT CONTROLLERS

Controller.	Area-1 (Δf_1)			Area-2 (Δf_2)			ΔP_{tie}		
	T_s (s)	MOS (mHz)	MUS (mHz)	T_s (s)	MOS (mHz)	MUS (mHz)	T_s (s)	MOS (mpu)	MUS (mpu)
FIMC-PID	8.420	-2.5	8.566	9.540	-4.2	2.8	14.562	-5	3.5
IMC-PID	9.185	-6.8	1.232	13.417	-9.2	2.1	17.488	0	7.8
PI	19.340	-6.3	13.89	19.595	-8.9	1.9	19.533	0	13
I	13.267	-7.3	20.92	17.799	-9.7	2.3	19.259	-6	7.1

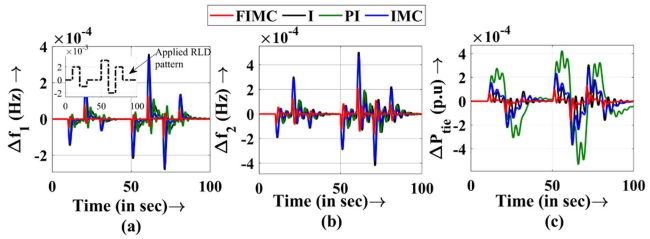

Fig. 11. Effect of RLD pattern on (a) frequency deflection in area-1, (b) Frequency deflection in area-2, and (c) deflection in tie-line power.

in Fig. 10. From Fig. 10, it is shown that the suggested controller exhibits improved transient and steady-state dynamics compared to that of the IMC-PID, PI, and I controller. In addition, the response generated by FIMC-PID is less oscillatory than that of others. Furthermore, the values of the values T_s, MOS, and MUS are greatly reduced (as seen in Table V).

Practical power systems are frequently subjected to random load disturbances (RLD). Therefore, the performance of the GJO-tuned FIMC strategy is examined using the RLD pattern shown in Fig. 12(a). This pattern is applied to the studied PS at the load points in both areas. The GJO-tuned FIMC-PID scheme gives better transient and steady-state properties with a significant reduction in oscillations. In other words, normality for the stated PS is quickly restored due to the performance of the GJO-tuned FIMC-PID strategy compared to other controllers (Fig. 11(a)–(c)).

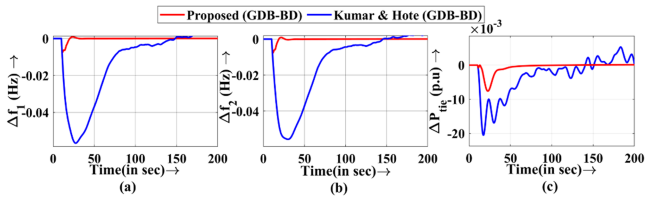

Fig. 12. Effect of thermal non-linearities on dynamic response: (a) deflection in frequency for area-1, (b) deflection in frequency for area-2, and (c) deflection in tie-line power.

TABLE VI
PERFORMANCE MEASURES AMID 30% PARAMETRIC ABERRATIONS

	Perturbation		-30%			+30%		
	Parameters	O/P	T_s (s)	MOS	MUS	T_s (s)	MOS	MUS
Thermal (Area-1)	τ_{g1}	Δf_1	6.34	0.3	-2.3	8.77	1.3	-2.8
		Δf_2	9.52	2.8	-4.2	10.3	2.8	-4.2
		ΔP_{tie}	14.4	3.5	-0.5	14.7	3.3	-0.5
	τ_{t1}	Δf_1	6.37	0.1	-0.2	7.36	1.5	-2.9
		Δf_2	9.51	2.8	-4.2	10.5	2.8	-4.2
		ΔP_{tie}	14.3	3.8	-0.6	15.3	2.9	-0.2
	H_1	Δf_1	6.97	1.5	-3.4	13.2	1.6	-0.2
		Δf_2	10.3	2.9	-4.2	9.77	2.7	-4.2
		ΔP_{tie}	14.4	3.9	-0.7	15.7	2.4	0.0
Thermal (Area-2)	τ_{g2}	Δf_1	6.37	0.8	-2.6	11.5	0.7	-2.6
		Δf_2	7.16	1.7	-3.8	19.0	3.9	-4.6
		ΔP_{tie}	15.6	2.7	0.0	19.3	4.3	-1.8
	τ_{t2}	Δf_1	5.19	0.9	-2.6	11.8	0.7	-2.6
		Δf_2	6.50	1.4	-3.7	19.5	4.2	-4.7
		ΔP_{tie}	16.3	2.2	0.0	19.4	4.7	-2.2
	H_2	Δf_1	7.22	0.9	-2.6	9.45	0.8	-2.5
		Δf_2	7.71	2.8	-4.9	14.8	2.8	-3.8
		ΔP_{tie}	15.3	2.9	0.0	16.0	4.0	-1.2

Units: Δf_1 and Δf_2 in mHz; ΔP_{tie} in mpu.

B. Perturbation Analysis

It is impracticable to obtain perfect PS models. Therefore, it is necessary to verify the robustness of the GJO-tuned FIMC controller when the parameters of the given plant model are perturbed. Here, a perturbation of +30% and −30% [4] is considered for the system parameters while retaining the controller settings given in Table I. Closed-loop performance measures such as T_s, MOS, and MUS amid 30% perturbation of various parameters of the power system are presented in Table VI. From this table, it is vindicated that the fluctuations in performance indices are not significant and the closed-loop response is stable. This indicates the robustness of the FIMC-PID design. In Table VI, Δf_1 and Δf_2 are expressed in mHz whereas ΔP_{tie} is expressed in mpu.

C. Performance During Presence of Thermal Non-Linearities

This section aims to analyze the system's performance considering boiler dynamics (BD) and governor dead band (GDB) [40] which are common sources of non-linearity in thermal power plants. These dynamics introduce real-time irregularities that arise from pressure controls, boiler storage, and the fuel injection system. To evaluate the impact of BD and GDB on dynamic performance, we compare the dynamic responses in the presence of these non-linearities to the PIDD2 strategy reported in [9]. As observed from Fig. 12, the GJO-tuned FIMC strategy exhibits

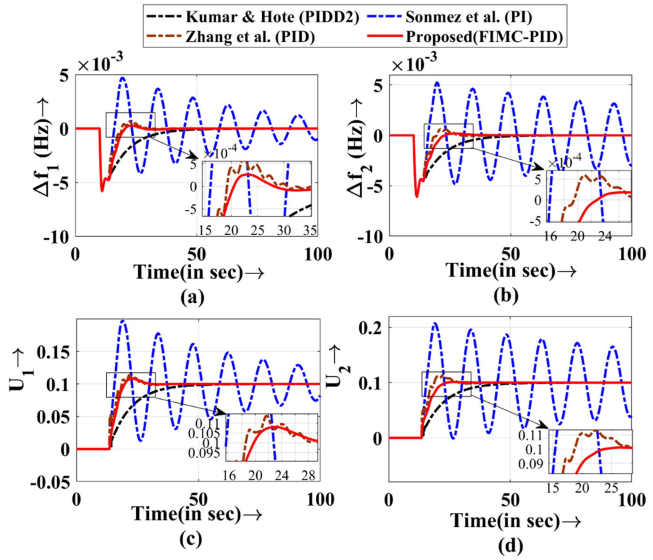

Fig. 13. Responses for with Delay: (a) frequency deflection in area-1, (b) frequency deflection in area-2, (c) control effort in area-1, and (d) control effort in area-2.

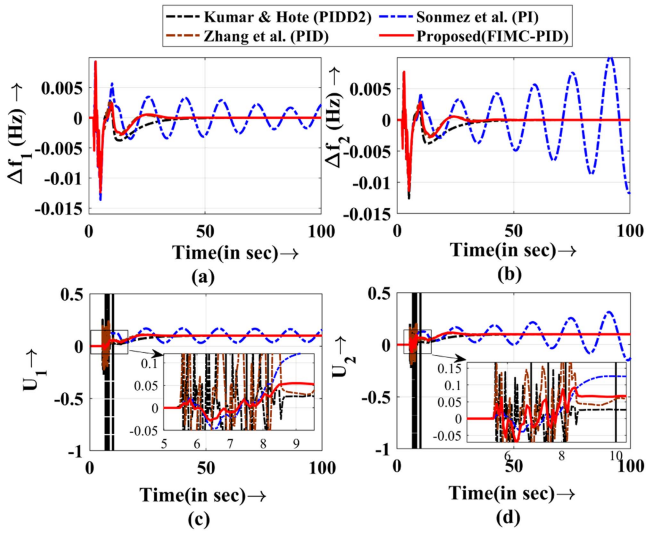

Fig. 14. Responses for location attack: (a) frequency deflection in area-1, (b) frequency deflection in area-2, (c) control effort in area-1, and (d) control effort in area-2.

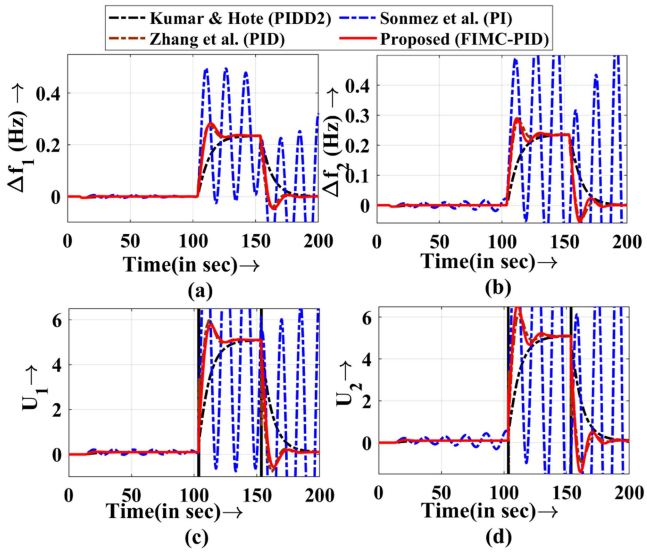

Fig. 15. Responses for data integrity (strategic) attack: (a) frequency deflection in area-1, (b) frequency deflection in area-2, (c) control effort in area-1, and (d) control effort in area-2.

superior performance to the PIDD2 strategy in managing nonlinearities.

D. Performance Evaluation Amid Cyber-Attacks and Delay

This section examines the effects of the attacks described in Section II-B on the performance of the GJO-tuned FIMC-PID strategy. For the simulation study, an inherent delay of $\theta = 3.5$ s is assumed in the LFC loop. Accordingly, the FIMC-PID controller settings are calculated as follows: $K_p = 0.1754$, $K_i = 0.4470$, $K_d = 0.1470$ (for area-1) and $K_p = 0.0210$, $K_i = 0.4061$, $K_d = 0.1760$ (for area-2). A load disturbance $\Delta P_{Li} = 0.1$ p.u is introduced at $t = 2$ s in both areas. In this section, the real signal is corrupted during all attacks, with manipulated data fed into specific locations of the CPS, as marked in Fig. 2. The FIMC-PID scheme is compared with PIDD2 of [9], PID of [13] and PI of [41] on the same power system model of [9]. The controller settings of these works are as follows: PIDD2 [9]: $K_{p1} = 0.0763, K_{d1} = 0.03, K_{i1} = 0.0804$, $K_{dd1} = 0.0061$, $K_{p2} = 0.0745$, $K_{d2} = 0.0293$, $K_{i2} = 0.0786$ and $K_{dd2} = 0.006$; PID [41]: $K_p = K_i = K_d = 0.2$ (in both areas); PI [13]: $K_p = 0.2$, $K_d = 0.4$ (in both areas).

1) Only Communication Delay: This case study can be treated as a 'no attack scenario' where only a delay (of 3.5 s) is considered as the potential challenge for the controller. The PI controller of Sonmez et al. [13] does not handle this delay and produces an oscillatory response. The PIDD2 of Kumar and Hote [9] and the PID of Zhang et al. [41] produce a stable response. PIDD2 [9] yields a slower response while PID [41] produces some undesirable overshoot as evident in Fig. 13. A similar trend is also observed in the control efforts comparison.

2) Location Attack: A location-based attack poses a substantial threat to the security and reliability of CPS. This attack is simulated using (12), where $t_1 = 2$ s, $t_2 = 3$ s, $t_3 = 5$ s, and $(\tau_a \in (3\,\text{s}, 5s))$, with $u(t)$ being a step input. $\lambda(t)$ represents an attack input that involves a uniformly distributed random number between -1 and 1 ($a = -1$ and $b = 1$). These attacks lead to sudden frequency deflections and tie-line power deviations, as shown in Fig. 14. However, the GJO-tuned FIMC effectively restores system stability, keeping frequency and power deviations within tolerable limits.

3) Strategic Attack (Data Integrity Attack): Under a strategic attack, an adversary alters the ACE channel to introduce a corrupted input in both areas. The manipulated version of ACE is obtained by adding a real number $\gamma = 5$ during the attack, which occurs within the duration $(\tau_a \in (100\,\text{s}, 150\,\text{s}))$, as stipulated in (15). The FIMC-PID controller's resilience to such strategic attacks is evident in Fig. 15, where the frequency and tie-line power deflections are quickly restored to normal.

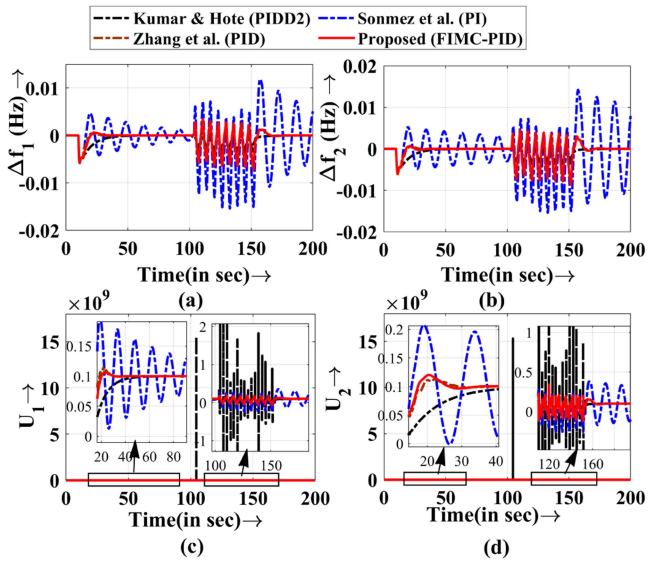

Fig. 16. Responses for resonance attack: (a) frequency deflection in area-1, (b) frequency deflection in area-2, (c) control effort in area-1, and (d) control effort in area-2.

Fig. 17. OPAL-RT based HIL test setup.

4) Resonance Attack: During a resonance attack, a specific value for $x_f = -0.5$ and a phase delay $\phi = -0.25$ are chosen to simulate (16). The improved resiliency of the GJO-tuned FIMC strategy in handling such resonance attacks with relatively smooth control action is evident in Fig. 16.

E. Hardware-in-the-Loop (HIL) Validation Study

This study scrutinizes the performance of the GJO tuned FIMC-PID controller in contrast to the IMC-based PIDD2 controller utilized in the work of [9]. Initial validation of the results is carried out in a MATLAB 2020a/Simulink environment, followed by real-time verification using the OPAL-RT OP5700 FPGA-based simulator (Fig. 17). This process aims to validate the initial simulation findings. To ensure a fair comparison, the PS employed by [9], along with the corresponding controller settings, is utilized. The GJO-tuned FIMC strategy is then redesigned for the same power system. The HIL validation includes three distinct scenarios: time delay, location attack with time delay, and strategic attack with time delay (each lasting 3.5 seconds).

1) Time Delay: The dynamic responses of frequency deviations and control efforts, as seen in Fig. 18, demonstrate that the proposed method achieves a faster settling time. Performance

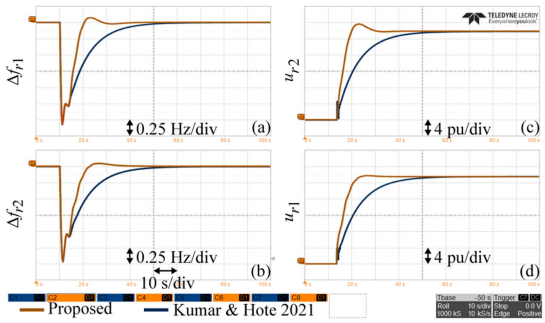

Fig. 18. Comparative HIL results obtained for time delay: (a) frequency deflection in area-1, (b) frequency deflection in area-2, (c) control effort in area-1, and (d) control effort in area-2.

TABLE VII
ACHIEVED PERCENTAGE IMPROVEMENT COMPARED TO [9]

Ts (sec)	PIDD2 [9]	FIMC-PID	Improvement
Δf_1 (mHz)	46.742	30.488	34.77%
Δf_2 (mHz)	46.260	33.183	28.26%
ΔP_{tie} (mpu)	80.591	52.461	34.90%

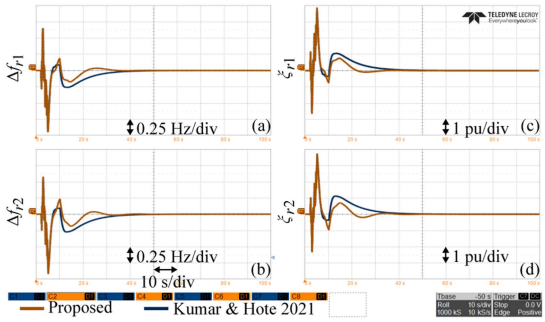

Fig. 19. Comparative HIL results obtained for location attack with time delay: (a) frequency deflection in area-1, (b) frequency deflection in area-2, (c) ACE in area-1, ξ_1 and (d) ACE in area-2, ξ_2.

improvements of the GJO-tuned FIMC strategy over the approach used in [9] are presented in Table VII.

2) Location Attack With Time Delay: In this scenario, the GJO-tuned FIMC strategy results in faster settling times for dual-area frequency deviations and ACE compared to the method used in [9], as evidenced in Fig. 19.

3) Strategic Attack With Time Delay: Under strategic attack conditions with time delay (as shown in Fig. 20), the GJO-tuned FIMC strategy continues to outperform the approach of [9] in terms of settling times for dual-area frequency deviations and ACE. It should be noted that the control effort for [9] is significantly higher, as seen in Fig. 21(a)–(d). However, in practical applications, smoother control action is preferred to prevent actuator saturation. This preference is satisfied by the GJO-tuned FIMC strategy, which provides a smoother control effort. Therefore, the GJO-tuned FIMC strategy exhibits superior resilience in dealing with location and strategic attacks, even when incorporating inherent delay.

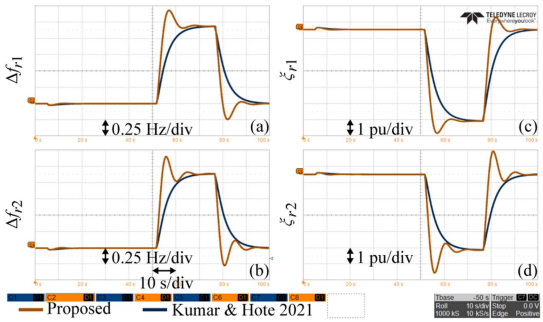

Fig. 20. Comparative HIL results obtained for strategic attack with time delay: (a) frequency deflection in area-1, (b) frequency deflection in area-2, (c) ACE in area-1, ξ_1, and (d) ACE in area-2, ξ_2.

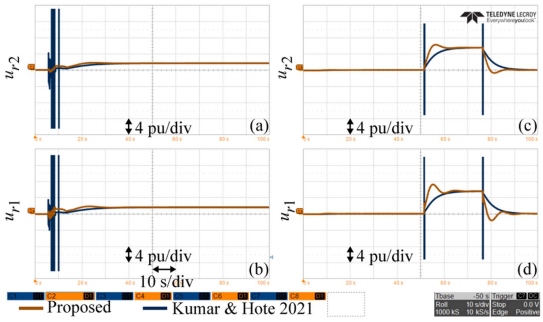

Fig. 21. Comparative HIL results obtained for location attack with time delay: (a) control effort in area-1, (b) control effort in area-2 for strategic attack with time delay, (c) control effort in area-1, and (d) control effort in area-2.

V. Conclusion and Future Scope

This article introduces a GJO-tuned FIMC strategy applied to a non-identical dual area thermal system. The approach demonstrates superior effectiveness in mitigating step and random load disturbances compared to existing controllers and optimizers. The proposed controller also demonstrates resilience against communication delays and cyber-attacks based on false data injection. Through hardware-based real-time validation, the GJO-tuned FIMC strategy exhibits performance improvements over a recent IMC-based PID controller with a double derivative strategy. In particular, it reduces the settling times of the frequency deflection response in area-1 and area-2 by 34.77% and 28.26%, respectively. Furthermore, it increases the settling time for tie line power deflection by 34.90% compared to the IMC-based PID strategy. Finally, the GJO-tuned FIMC's capacity to counter location and strategic attacks, despite significant inherent delays, is affirmed through the OPAL-RT platform.

It is crucial to recognize the extensive and ever-expanding range of attacks. Therefore, it may be challenging to assert definitively that our proposed method can handle all potential cyber-attacks. There could be certain types of attack from the denial-of-service category where the proposed method may not be effective. Moreover, the present work can be extended to deal with unknown disturbances by employing suitable estimation techniques.

References

[1] P. Aryan and G. L. Raja, "Analysis of type-2 fuzzy $I^{\lambda}D^{\mu} - P$ controller for LFC with communication delay," in *Proc. IEEE Glob. Conf. Comput. Power Commun. Technol.*, 2022, pp. 01–07.

[2] N. R. Babu, S. K. Bhagat, L. C. Saikia, T. Chiranjeevi, R. Devarapalli, and F. P. G. Márquez, "A comprehensive review of recent strategies on automatic generation control/load frequency control in power systems," *Arch. Comput. Methods Eng.*, vol. 30, pp. 543–572, 2023.

[3] N. Kumari, P. Aryan, G. L. Raja, and Y. Arya, "Dual degree branched type-2 fuzzy controller optimized with a hybrid algorithm for frequency regulation in a triple-area power system integrated with renewable sources," *Protection Control Modern Power Syst.*, vol. 8, no. 3, pp. 1–29, Jul. 2023.

[4] A. Anand, P. Aryan, N. Kumari, and G. L. Raja, "Type-2 fuzzy-based branched controller tuned using arithmetic optimizer for load frequency control," *Energy Sources Part A Recovery Utilization Environ. Effects*, vol. 44, no. 2, pp. 4575–4596, 2022.

[5] P. Aryan and G. L. Raja, "Design and analysis of novel QOEO optimized parallel fuzzy FOPI-PIDN controller for restructured AGC with HVDC and PEV," *Iranian J. Sci. Technol. Trans. Elect. Eng.*, vol. 46, no. 2, pp. 565–587, 2022.

[6] M. Ranjan and R. Shankar, "A literature survey on load frequency control considering renewable energy integration in power system: Recent trends and future prospects," *J. Energy Storage*, vol. 45, 2022, Art. no. 103717.

[7] A. Ghosh, A. K. Ray, O. Singh, and M. Jamshidi, "Optimized load frequency controller performances with a reduced number of decision variables: A gravitational search algorithm-based method," *IEEE Syst., Man, Cybern. Mag.*, vol. 9, no. 1, pp. 48–57, Jan. 2023.

[8] B. Abdollahzadeh, F. S. Gharehchopogh, and S. Mirjalili, "African vultures optimization algorithm: A new nature-inspired metaheuristic algorithm for global optimization problems," *Comput. Ind. Eng.*, vol. 158, 2021, Art. no. 107408.

[9] M. Kumar and Y. V. Hote, "Robust PIDD2 controller design for perturbed load frequency control of an interconnected time-delayed power systems," *IEEE Trans. Control Syst. Technol.*, vol. 29, no. 6, pp. 2662–2669, Nov. 2021.

[10] P. Dehuri and Y. V. Hote, "Indirect IMC based PID controller design for single area LFC system in the presence of uncertainty and communication delay," in *Proc. IEEE Texas Power Energy Conf.*, 2021, pp. 1–6.

[11] D. G. Padhan and S. Majhi, "A new control scheme for PID load frequency controller of single-area and multi-area power systems," *ISA Trans.*, vol. 52, no. 2, pp. 242–251, 2013.

[12] M. N. Anwar and S. Pan, "A new PID load frequency controller design method in frequency domain through direct synthesis approach," *Int. J. Elect. Power Energy Syst.*, vol. 67, pp. 560–569, 2015.

[13] Ş. Sönmez, S. Ayasun, and C. O. Nwankpa, "An exact method for computing delay margin for stability of load frequency control systems with constant communication delays," *IEEE Trans. Power Syst.*, vol. 31, no. 1, pp. 370–377, Jan. 2016.

[14] P. Aryan, G. L. Raja, R. Vilanova, and M. Meneses, "Repositioned internal model control strategy on time-delayed industrial processes with inverse behavior using equilibrium optimizer," *IEEE Access*, vol. 11, pp. 54556–54568, 2023.

[15] Y. Jiang, S. Wu, R. Ma, M. Liu, H. Luo, and O. Kaynak, "Monitoring and defense of industrial cyber-physical systems under typical attacks: From a systems and control perspective," *IEEE Trans. Ind. Cyber- Phys. Syst.*, vol. 1, pp. 192–207, 2023.

[16] M. Ghiasi, T. Niknam, Z. Wang, M. Mehrandezh, M. Dehghani, and N. Ghadimi, "A comprehensive review of cyber-attacks and defense mechanisms for improving security in smart grid energy systems: Past, present and future," *Electric Power Syst. Res.*, vol. 215, 2023, Art. no. 108975.

[17] X. Wang, Y. Zhou, B. Luo, Y. Jiang, and T. Huang, "Event-triggered adaptive finite-time control for switched cyberphysical systems with uncertain deception attacks," *IEEE Trans. Ind. Cyber- Phys. Syst.*, vol. 1, pp. 136–146, 2023.

[18] V. S. Rajkumar, A. Ştefanov, A. Presekal, P. Palensky, and J. L. R. Torres, "Cyber attacks on power grids: Causes and propagation of cascading failures," *IEEE Access*, vol. 11, pp. 103154–103176, 2023.

[19] P. Chen, D. Zhang, L. Yu, and H. Yan, "Dynamic event-triggered output feedback control for load frequency control in power systems with multiple cyber attacks," *IEEE Trans. Syst., Man, Cybern. Syst.*, vol. 52, no. 10, pp. 6246–6258, Oct. 2022.

[20] S. Hu, X. Ge, X. Chen, and D. Yue, "Resilient load frequency control of islanded AC microgrids under concurrent false data injection and denial-of-service attacks," *IEEE Trans. Smart Grid*, vol. 14, no. 1, pp. 690–700, Jan. 2023.
[21] Y. Wu, Z. Wei, J. Weng, X. Li, and R. H. Deng, "Resonance attacks on load frequency control of smart grids," *IEEE Trans. Smart Grid*, vol. 9, no. 5, pp. 4490–4502, Sep. 2018.
[22] X. Wang, D. Ding, H. Dong, and X. Yi, "PI-based security control against joint sensor and controller attacks and applications in load frequency control," *IEEE Trans. Syst., Man, Cybern. Syst.*, vol. 53, no. 2, pp. 970–980, Feb. 2023.
[23] G. Zhang, J. Li, O. Bamisile, Y. Xing, D. Cai, and Q. Huang, "An H load frequency control scheme for multi-area power system under cyber-attacks and time-varying delays," *IEEE Trans. Power Syst.*, vol. 38, no. 2, pp. 1336–1349, Mar. 2023.
[24] S. Ahmad and H. Ahmed, "Robust intrusion detection for resilience enhancement of industrial control systems: An extended state observer approach," *IEEE Trans. Ind. Appl.*, vol. 59, no. 6, pp. 7735–7743, Nov./Dec. 2023.
[25] X. Zhao, Z. Ma, S. Li, and S. Zou, "Robust LFC of power systems with wind power under packet losses and communication delays," *IEEE Trans. Emerg. Sel. Topics Circuits Syst.*, vol. 12, no. 1, pp. 135–148, Mar. 2022.
[26] H. Shen, Y. Xia, J. Wang, and J. H. Park, "Fault-tolerant event-triggered $\mathcal{H}_\infty$ load frequency control for multiarea power systems with communication delay," *IEEE Syst. J.*, vol. 16, no. 4, pp. 6624–6634, Dec. 2022.
[27] S. Yan, Z. Gu, J. H. Park, X. Xie, and C. Dou, "Probability-density-dependent load frequency control of power systems with random delays and cyber-attacks via circuital implementation," *IEEE Trans. Smart Grid*, vol. 13, no. 6, pp. 4837–4847, Nov. 2022.
[28] M. Kumar, "Resilient PIDA control design based frequency regulation of interconnected time-delayed microgrid under cyber-attacks," *IEEE Trans. Ind. Appl.*, vol. 59, no. 1, pp. 492–502, Jan./Feb. 2023.
[29] A. M. Mohan, N. Meskin, and H. Mehrjerdi, "A comprehensive review of the cyber-attacks and cyber-security on load frequency control of power systems," *Energies*, vol. 13, no. 15, 2020, Art. no. 3860.
[30] B. Verma and P. K. Padhy, "Indirect IMC-PID controller design," *IET Control Theory Appl.*, vol. 13, no. 2, pp. 297–305, 2019.
[31] N. Chopra and M. M. Ansari, "Golden jackal optimization: A novel nature-inspired optimizer for engineering applications," *Expert Syst. Appl.*, vol. 198, 2022, Art. no. 116924.
[32] H. Saadat, *Power System Analysis*. New York, NY, USA: McGraw Hill, 1999.
[33] B. Verma and P. K. Padhy, "Optimal PID controller design with adjustable maximum sensitivity," *IET Control Theory Appl.*, vol. 12, no. 8, pp. 1156–1165, 2018.
[34] S. Skogestad, "Simple analytic rules for model reduction and PID controller tuning," *J. Process Control*, vol. 13, no. 4, pp. 291–309, 2003.
[35] S. Saxena and Y. V. Hote, "Load frequency control in power systems via internal model control scheme and model-order reduction," *IEEE Trans. Power Syst.*, vol. 28, no. 3, pp. 2749–2757, Aug. 2013.
[36] Z. Zhen et al., "Pattern classification and PSO optimal weights based sky images cloud motion speed calculation method for solar PV power forecasting," *IEEE Trans. Ind. Appl.*, vol. 55, no. 4, pp. 3331–3342, Jul./Aug. 2019.
[37] M. A. Hannan et al., "Particle swarm optimization algorithm based fuzzy controller for solid-state transfer switch toward fast power transfer and power quality mitigation," *IEEE Trans. Ind. Appl.*, vol. 59, no. 5, pp. 5570–5579, Sep./Oct. 2023.
[38] D. Wang, C. Fu, Q. Zhao, and T. Hu, "A PSO-based optimization design of W-type noncontact transformer for stable power transfer in DWPT system," *IEEE Trans. Ind. Appl.*, vol. 58, no. 1, pp. 1211–1221, Jan./Feb. 2022.
[39] S. M. H. Mousakazemi, "Comparison of the error-integral performance indexes in a GA-tuned PID controlling system of a PWR-type nuclear reactor point-kinetics model," *Prog. Nucl. Energy*, vol. 132, 2021, Art. no. 103604.
[40] S. Gupta, *Power System Operation Control & Restructuring*. New Delhi, Delhi, India: IK Int., 2015.
[41] C.-K. Zhang, L. Jiang, Q. Wu, Y. He, and M. Wu, "Further results on delay-dependent stability of multi-area load frequency control," *IEEE Trans. Power Syst.*, vol. 28, no. 4, pp. 4465–4474, Nov. 2013.

Nikhil Kumar received the B.Tech. degree in electrical and electronics engineering from Guru Gobind Singh Indraprastha University, Delhi, India, and the M.Tech degree in control systems from the National Institute of Technology, Patna, India. His engagement is as Traction Software Development Engineer in the traction control wing at Alstom. His research focuses on model-based analytical load frequency regulation schemes.

Pulakraj Aryan (Graduate Student Member, IEEE) received the B.E. degree in electrical and electronics engineering from the Birla Institute of Technology, Mesra, Ranchi, India, in 2016, and the M.Tech. and Ph.D. degrees in control systems from the National Institute of Technology, Patna, India, in 2020 and 2023, respectively. He is currently a Research Associate with the Hydropower Simulation Lab, Center for Sustainable Energy, IIT Roorkee, Roorkee, India. He has authored several book chapters and has more than 20 publications in peer-reviewed international conference proceedings and reputed journals. His research focuses on hack-free hydroplant control systems.

G. Lloyds Raja (Member, IEEE) received the B.E. and M.E. degrees from Anna University, Chennai, India, in 2009 and 2011, respectively, and the Ph.D. degree from the Indian Institute of Technology Patna, Patna, India, in 2018. He was with the Department of Automation, Shanghai Jiao Tong University, Shanghai, China, for a short period as a Postdoctoral Researcher. He is currently an Assistant Professor with the Department of Electrical Engineering, National Institute of Technology, Patna, India. He has authored several book chapters and has more than 35 publications in peer-reviewed international conference proceedings and reputed journals. His research interests include chemical process control and advanced load frequency control strategies.

Utkal Ranjan Muduli (Senior Member, IEEE) received the B.Tech. degree in electrical and electronics engineering from the Biju Patnaik University of Technology, Rourkela, India, in 2011, the M.Tech. degree in electrical engineering from the Indian Institute of Technology Gandhinagar, Gandhinagar, India, in 2014, and the Ph.D. degree in electrical engineering from the Indian Institute of Technology Patna, Patna, India, in 2022. He was a Visiting Scholar and Research Associate with the Department of Electrical Engineering and Computer Science, Khalifa University, Abu Dhabi, UAE, in 2019 and 2021, respectively, where he is currently a Postdoctoral Research Fellow. His research interests include modulation strategies for multiphase motor drives, matrix converters and its control, battery power management, and wireless power transfer. He was the recipient of the 2022 IEEE Outstanding Paper Award for IEEE Transactions on Industrial Electronics.